catalysts

MDPI

Article

$BaCO_3$ Nanoparticles-Modified Composite Cathode with Improved Electrochemical Oxygen Reduction Kinetics for High-Performing Ceramic Fuel Cells

Halefom G. Desta [1,2,3], Quan Yang [3], Dong Tian [3], Shiyue Zhu [3], Xiaoyong Lu [3], Kai Song [3], Yang Yang [4], Yonghong Chen [3], Baihai Li [2] and Bin Lin [1,2,3,*]

[1] School of Mechanical and Electrical Engineering, School of Materials and Energy, University of Electronic Science and Technology of China, Chengdu 611731, China
[2] Yangtze Delta Region Institute (Huzhou), University of Electronic Science and Technology of China, Huzhou 313001, China
[3] Anhui Key Laboratory of Low-Temperature Co-Fired Material, Huainan Engineering Research Center for Fuel Cells, Huainan Normal University, Huainan 232001, China
[4] School of Materials Science and Physics, China University of Mining and Technology, Xuzhou 221116, China
* Correspondence: bin@uestc.edu.cn

Abstract: The effects of the electrochemical oxygen reduction reaction (ORR) on the surface of single-phase perovskite cathodes are well understood, but its potential for use in a complex system consisting of different material types is unexplored. Herein, we report how $BaCO_3$ nanoparticles-modified $La_{0.6}Sr_{0.4}Co_{0.2}Fe_{0.8}O_{3-\delta}$-$Gd_{0.2}Ce_{0.8}O_{2-\delta}$ (LSCF–GDC)-composite cathodes improved the electrochemical oxygen reduction kinetics for high-performing ceramic fuel cells. Both X-ray diffraction (XRD) and thermogravimetric analysis (TGA) studies reveal that $BaCO_3$ is stable, and that it does not show any solid-state reaction with LSCF–GDC at SOFCs' required operating temperature. The electrochemical conductivity relaxation (ECR) study reveals that during the infiltration of $BaCO_3$ nanoparticles into LSCF–GDC, the surface exchange kinetics (K_{chem}) are enhanced up to a factor of 26.73. The maximum power density of the NiO-YSZ anode-support cell is increased from 1.08 to 1.48 W/cm^2 via surface modification at 750 °C. The modified cathode also shows an ultralow polarization resistance (R_p) of 0.027 Ω.cm^2, which is ~4.4 times lower than that of the bare cathode (~0.12 Ω.cm^2) at 750 °C. Such enhancement can be attributed to the accelerated oxygen surface exchange process, possibly through promoting the dissociation of oxygen molecules via the infiltration of $BaCO_3$ nanoparticles. The density functional theory (DFT) illustrates the interaction mechanism between oxygen molecules and the $BaCO_3$ surface.

Keywords: SOFCs; surface infiltration; oxygen reduction reaction; high power density

Citation: Desta, H.G.; Yang, Q.; Tian, D.; Zhu, S.; Lu, X.; Song, K.; Yang, Y.; Chen, Y.; Li, B.; Lin, B. $BaCO_3$ Nanoparticles-Modified Composite Cathode with Improved Electrochemical Oxygen Reduction Kinetics for High-Performing Ceramic Fuel Cells. *Catalysts* **2022**, *12*, 1046. https://doi.org/10.3390/catal12091046

Academic Editors: Yuxin Tang and Jianping Yang

Received: 21 August 2022
Accepted: 8 September 2022
Published: 14 September 2022

1. Introduction

Solid oxide fuel cells (SOFCs) are among the cleanest and most highly efficient forms of chemical energy storage, which can convert a variety of fuels into electrical energy. But regardless of their many advantages, SOFCs only exhibit sufficiently high performance at high temperatures (>800 °C) [1–4]. Thus, the practical application of SOFC technology is hindered by its high operating temperature requirement, which induces various issues such as high manufacturing costs, materials degradation, and slow startup/shutdown cycles. Currently, researchers are mainly focused on mitigating these problems by reducing the SOFCs' operating temperature to a temperature below 800 °C [5–8]. Unfortunately, reducing the operating temperature typically leads to sluggish oxygen reduction reaction (ORR) kinetics, thereby hindering the overall SOFC output performance [9–12]. Therefore, the availability of cathode materials with high ORR activity at reduced temperatures is critical for promoting the commercialization of SOFC technology.

Recently, perovskite-type oxides (La, Sr) (Co, Fe) O_3 (LSCF) have been widely studied as the state-of-the-art cathode materials for the operation of SOFCs at reduced temperatures, due to their high electrical and satisfactory ionic conductivity properties. Considering the high oxygen-ion-conducting and adequate thermal expansion coefficient (TEC), the incorporation of rare-earth-doped ceria into cathode materials leads to further enhanced three-phase boundary (TPB) pathways for the ORR. Among the incorporated doped ceria, the $La_{0.6}Sr_{0.4}Co_{0.2}Fe_{0.8}O_{3-\delta}$-$Gd_{0.2}Ce_{0.8}O_{2-\delta}$ (LSCF–GDC) composite cathode is one of the most extensively studied candidates for IT-SOFCs applications [7,13–17]. However, the surface oxygen exchange kinetics are still slow at reduced temperatures. In this regard, it is desirable to enhance the surface oxygen exchange kinetics at reduced temperatures.

Modifying the surface of cathode materials is an efficient technique for enhancing the electrochemical performance of SOFCs at reduced operating temperatures, without changing the pre-existing merits of the backbone materials [18]. Recently, wide efforts have been devoted to surface modification of cathode materials via solution-based infiltration for enhancing the performance of SOFCs [19–22]. Several suitable catalysts/materials have been investigated for surface modifications of LSCF | LSCF–GDC cathode materials to enhance the ORR activity, including mixed ionic-electronic conductors (MIECs) [23–25], noble metals [26,27], and transition metal oxides [28–31].

More recent studies have also shown that the catalytic activity of cathode materials was significantly improved by the infiltration of non-ionic/electronic conducting phases, such as alkali earth metal compounds, into the surface. Additionally, alkali earth metal compounds are low-cost and widely available [32–34]. For example, Lu Zhang et al. [35] reported a peak power density of 0.835 W/cm^2 at 650 °C for a NiO-SDC anode-support single with a 2.47 wt.% CaO-modified LSCF-SDC cathode, which is much higher than that of the pristine cathode (0.622 W/cm^2). Similarly, Tao Hong et al. [36] reported a peak power density of 0.73 W/cm^2 at 700 °C on a surface-modified LSCF cathode with $BaCO_3$. Moreover, our recent work also shows that the performance of NiO-YSZ-anode-supported cells based on the LSF-GDC composite cathode is greatly enhanced from 0.712 to 0.993 W/cm^2 at 750 °C via the impregnation of $BaCO_3$ nanoparticles [37]. However, to the best of our knowledge, the origin of the catalytic mechanisms of $BaCO_3$ for ORR is still not well understood. In this context, this work deals with the infiltration of $BaCO_3$ nanoparticles into the surface of the LSCF–GDC composite cathode to investigate the catalytic mechanism of $BaCO_3$ for ORR at reduced temperatures.

Herein, we report on $BaCO_3$ nanoparticles-modified $La_{0.6}Sr_{0.4}Co_{0.2}Fe_{0.8}O_{3-\delta}$-$Gd_{0.2}Ce_{0.8}O_{2-\delta}$ (LSCF–GDC) composite cathodes with improved electrochemical oxygen reduction kinetics for high-performing ceramic fuel cells. $BaCO_3$ nanoparticles were prepared via solution-based infiltration of barium acetate (Ba-$(OAc)_2$) as a precursor into the LSCF–GDC surface and followed by heating at 750 °C for 2 h (Figure 1). Furthermore, using the first-principle method, the interaction mechanism between the oxygen molecules and the $BaCO_3$ surface is clarified. As a result, the modified cathodes can significantly enhance the performance of single-cell and symmetrical cells at reduced temperatures.

Figure 1. Schematic figure of the Barium Acetate (Ba-$(OAc)_2$) infiltration into the surface of LSCF–GDC composite cathode.

2. Results and Discussion

Figure 2a shows the thermogravimetric analysis (TGA) of Ba-$(OAc)_2$ conducted in the air from 25 to 750 °C. The thermal decomposition temperature of Ba-$(OAc)_2$ starts at ~435 °C and ends up at ~520 °C. The total weight loss is ~22.58%, which can be associated with the evaporation of moisture (H_2O) and carbon dioxide (CO_2). The weight loss

percentage is nearly close to the theoretical value of 22.75% for the Ba-$(OAc)_2$ thermal decomposition [34,38]. No extra weight change is observed from 520 to 750 °C, demonstrating that Ba-$(OAc)_2$ is completely decomposed at ~520 °C, and kept stable at this operating temperature.

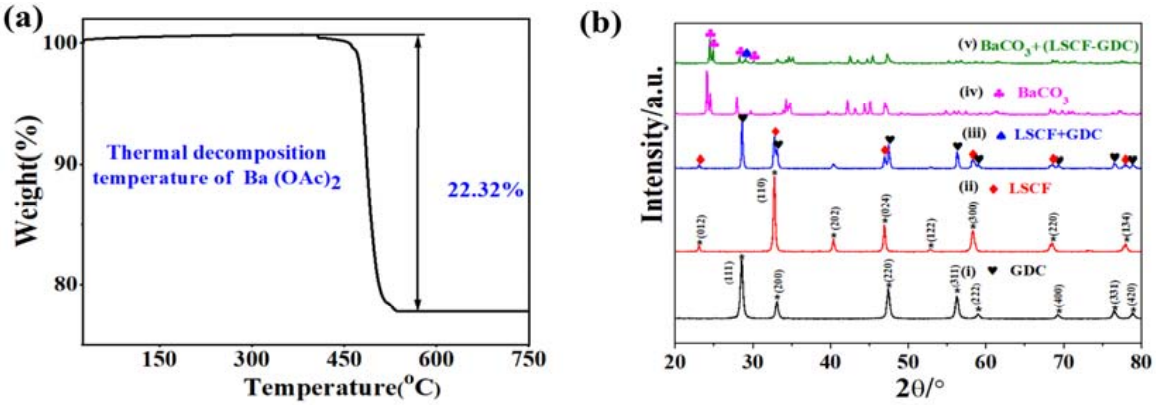

Figure 2. (**a**) TG curve for Ba-$(OAc)_2$ measured in air, (**b**) XRD patterns of GDC, LSCF, and chemical compatibility composite powders.

Figure 2b displays the XRD pattern of as-prepared pure powders and the chemical compatibility of composite powders. Figure 2b(i) shows the XRD peaks of the GDC powder calcined at 700 °C and exhibiting cubic fluorite phase with space group Fm-3m. The single-phase LCSF was obtained after calcination at 1000 °C and exhibited an orthorhombic phase perovskite structure with space group R-3c, as displayed in Figure 2b(ii). Meanwhile, for the chemical compatibility study, LSCF–GDC was mixed at a 50:50, weight ratio, followed by co-heating at 1000 °C for 5 h. The XRD peaks of LSCF + GDC composite powders exhibited two main structure phases corresponding to GDC and LSCF, as shown in Figure 2b(iii). The results confirmed that LSCF is chemically compatible with GDC; since no additional peaks appearing between LSCF and GDC were detected. The XRD patterns of the Ba-$(OAc)_2$, which was thermally heated at 750 °C, for 2 h to form an orthorhombic structured $BaCO_3$ with space group Pnma (PDF card number: 41-0373), confirmed the successful formation of $BaCO_3$, as displayed in Figure 2b(iv). Moreover, we also studied the chemical compatibility of composite powder $BaCO_3$ | (LSCF–GDC) (50:50 weight ratio) after being co-heated at 750 °C for 5 h in air. All diffraction peaks are associated with either of the starting powders $BaCO_3$ | (LSCF–GDC) without any impurities as presented in Figure 2b(v). These results demonstrate that Ba-$(OAc)_2$ decomposes to $BaCO_3$ in the presence of LSCF–GDC and shows good chemical compatibility between the $BaCO_3$ and (LSCF–GDC) at the operating conduction.

The microstructure of the single cell based on the $BaCO_3$ modified LSCF-GDC cathode is presented in Figure 3. The dense YSZ electrolyte, ~19 μm in thickness, is well-adhered to both the GDC buffer layer and the NiO-YSZ anode without any connected pores or cracks, as displayed in Figure 3a. The thicknesses of the buffer layer and anode are aapproximeee~2 and~40 μm, respectively. The microstructure of the targeted cathode adhered well to the buffer layer, thereby preventing direct contact between the LSCF–GDC and YSZ. As shown in Figure 3b, $BaCO_3$ nanoparticles are homogeneously distributed on the surface of the cathode without changing the porosity of the pre-existing cathode. The presence of $BaCO_3$ on the surface of the LSCF–GDC cathode is also analyzed using energy-dispersive spectroscopy (EDS), as shown in Figure 4. All elements, including La, Sr, Co, Fe, Ce, Gd, Ba, C, and O, are evenly distributed within the surface-modified LSCF–GDC cathode. Hence, Ba and C are incorporated on the surface of the cathode, confirming that the $BaCO_3$ has been successfully incorporated into the surface of the LSCF–GDC cathode after infiltration of the Ba-$(OAc)_2$ solutions.

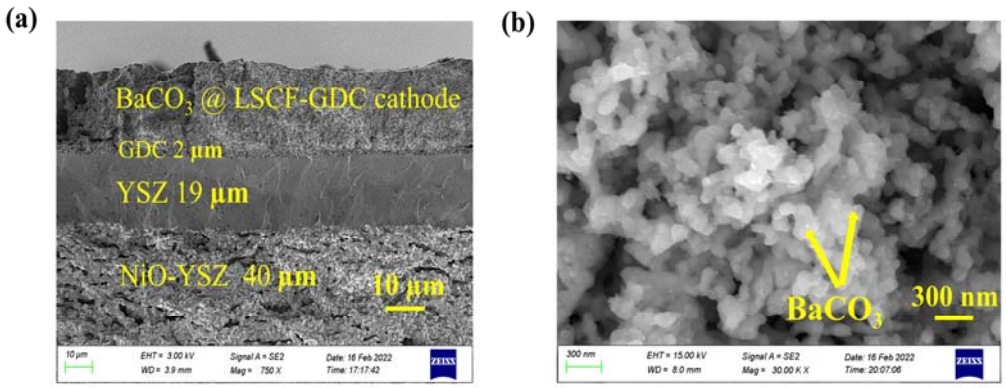

Figure 3. SEM images of (**a**) anode-supported single-cell, and (**b**) $BaCO_3$ nanoparticle infiltrated LSCF–GDC cathode.

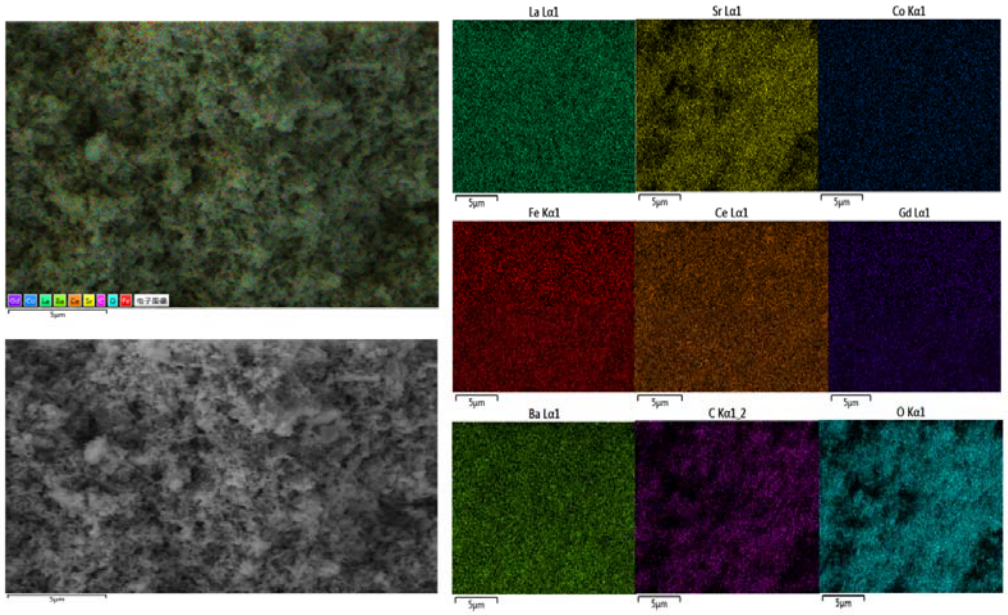

Figure 4. Energy-dispersive spectroscopy (EDS) elements mapping result of $BaCO_3$ infiltrated LSCF–GDC.

Figure 5 shows the normalized conductivity relaxation transients of bare LSCF–GDC and 0.065 mg/cm^2 $BaCO_3$ infiltrated LSCF–GDC at 750 °C, upon the step-change atmosphere from $P(O_2)$ = 0.20 atm (O_2 + N_2) to $P(O_2)$ = 1.0 atm (O_2), via controlling a mixture of O_2 and N_2. The change in ECR, indicates the change in the oxygen concentration of the sample, after shifting the partial P (O_2). The elapsed time to reach re-equilibrium for the bare LSCF–GDC is about 9000 s, while for the modified LSCF–GDC, is reduced to 350 s. The decreased re-equilibrium time confirmed an enhanced surface oxygen exchange process since the oxygen bulk-diffusion properties of the sample could remain unchanged by the surface modification. The surface oxygen reduction kinetics (K_{chem}) were derived from the ECR curve and the data were fitted using MATLAB software. The derived K_{chem} value of the bare is 3.03×10^{-5} cm·s^{-1} at 750 °C, which is comparable with previously reported values of LSCF [32,33]. The K_{chem} value of the modified LSCF–GDC is 8.1×10^{-4} cm·s^{-1}, which is a roughly 26.73-fold improvement. This result is consistent with the theoretical results which suggest that the infiltration of $BaCO_3$ improves the dissociation of oxygen molecules, thereby accelerating the oxygen reduction kinetics (K_{chem}).

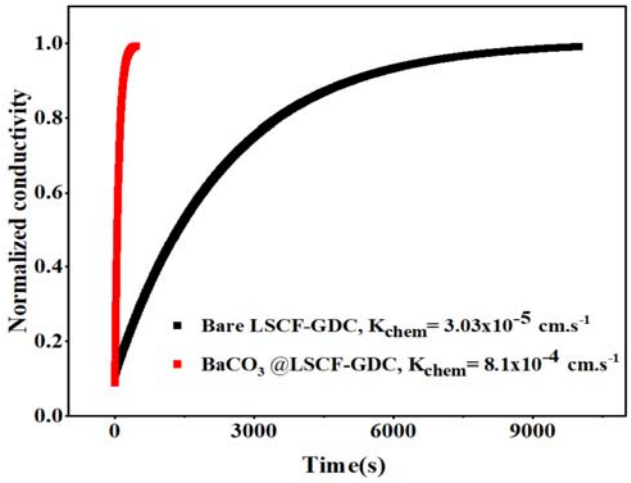

Figure 5. The electrochemical conductivity relaxation (ECR) curves bare LSCF–GDC and 0.065 mg/cm^2 $BaCO_3$ modified LSCF–GDC after a sudden shift of the P (O_2) from 0.2 to 1 atm at 750 °C.

The polarization resistance (R_p) of the cathodes is studied using a symmetrical cell configuration, i.e., LSCF–GDC | GDC | YSZ | GDC | LSCF–GDC. An electrical equivalent circuit model, L-R_o-(R_HQ_H)-(R_LQ_L) was fitted with the experimental EIS data, where L, R, and Q, represent the inductance, resistance, and constant phase, respectively, and where the subscripts H and L correspond to the high- and low-frequency arc resistances, respectively. The intercept of the Nyquist plots on the real axis at high frequency corresponds to ohmic resistance, while the intercept at low frequency corresponds to the total resistance. The difference between the ohmic resistance and total resistance is equivalent to the polarization resistance (R_p) of the cathode. For a simple comparison of the cathode performance, the ohmic resistance was deducted from the spectra. The calculated R_p values of the modified cathode are 0.027, 0.037, 0.043, and 0.12 Ω.cm^2 for 8.26, 5.64, 11 wt.% $BaCO_3$ and bare LSCF–GDC at 750 °C, respectively, as shown in Figure 6a. The R_p value of the bare LSCF–GDC cathode reported in this study is comparable with the value reported in the literature [39,40]. As shown in Figure 6c, the modified cathode shows a significant decrease in R_p values over the temperature ranges of 600 to 750 °C, compared to the bare cathode. The significant decrease in R_p can be attributed to the infiltration of $BaCO_3$ nanoparticles, which improves the dissociation of oxygen molecules. The lowest R_p values are obtained with moderate loading of 8.26 wt.% $BaCO_3$ at different temperatures. For example, the R_p value with 8.26 wt.% $BaCO_3$ loading decreases from 0.12 to 0.027 Ω·cm^2 (~4.4 times reduced) at 750 °C, and from 0.27 to 0.09 Ω·cm^2 (~3 times) at 700 °C. However, when the loading of $BaCO_3$ nanoparticles is further increased to 11 wt.%, which leads to an increase in the R_p from 0.027 to 0.043 Ω·cm^2, this can be associated with the blocking of the active pore of the cathode with $BaCO_3$, thereby leading to a delay of the diffusion of oxygen to the active area. Figure 6d shows the temperature dependence of the R_p values for different $BaCO_3$ loadings and the corresponding activation energy (Ea) calculated from the slope of the Arrhenius plots. The activation energy of the moderate loading of 8.26 wt.% $BaCO_3$ is 1.23 eV, which is lower than the activation energy of the bare LSCF–GDC cathode (1.48 eV), demonstrating that the oxygen reduction process is effectively enhanced after being modified with $BaCO_3$ nanoparticles.

To evaluate the performance of cathodes in SOFCs, a NiO-YSZ-based anode-supported cell was fabricated using a YSZ | GDC bilayer electrolyte, which prevents the formation of the insulating phase by blocking direct contact between LSCF–GDC and YSZ electrolytes. Figure 7 displays the typical I–V and I–P curves of single-cells measured between 600 °C and 750 °C, where wet H_2 (~3% H_2O) as fuel was provided to the anode side and the ambient air at the cathode side. The OCV values of both cells were between ~1.00–1.02 V, which is nearly close to the theoretical values obtained from the Nernst equation. The

maximum power densities (MPD) achieved for $BaCO_3$-modified LSCF–GDC cathode-based single cells are 1.48, 1.26, 0.94, and 0.61 W/cm^2 at 750, 700, 650, and 600 °C, respectively, as shown in Figure 7a. However, the maximum power densities of bare LSCF–GDC cathode-based single cells are 1.08, 0.840, 0.6, and 0.4 W/cm^2 at the corresponding temperature, as displayed in Figure 7b, which is comparable to the highest reported values of the NiO-YSZ-based anode-supported cell with a LSCF–GDC cathode [41,42]. As expected, the cell with the $BaCO_3$ modified cathode exhibited superior performance compared to the bare cathode-based cell, as shown in Figure 7c. For example, the maximum power density of the cell based on the $BaCO_3$ modified cathodes is 1.48 W/cm^2 at 750 °C, whereas the maximum power density of the cell based on the bare cathode is, 1.08 W/cm^2, implying a 37% increase in the maximum power densities. Since both cells have the same electrolytes and anodes, such a noticeable enhancement of cell performance at reduced temperatures is predominantly attributed to the improved cathode performance.

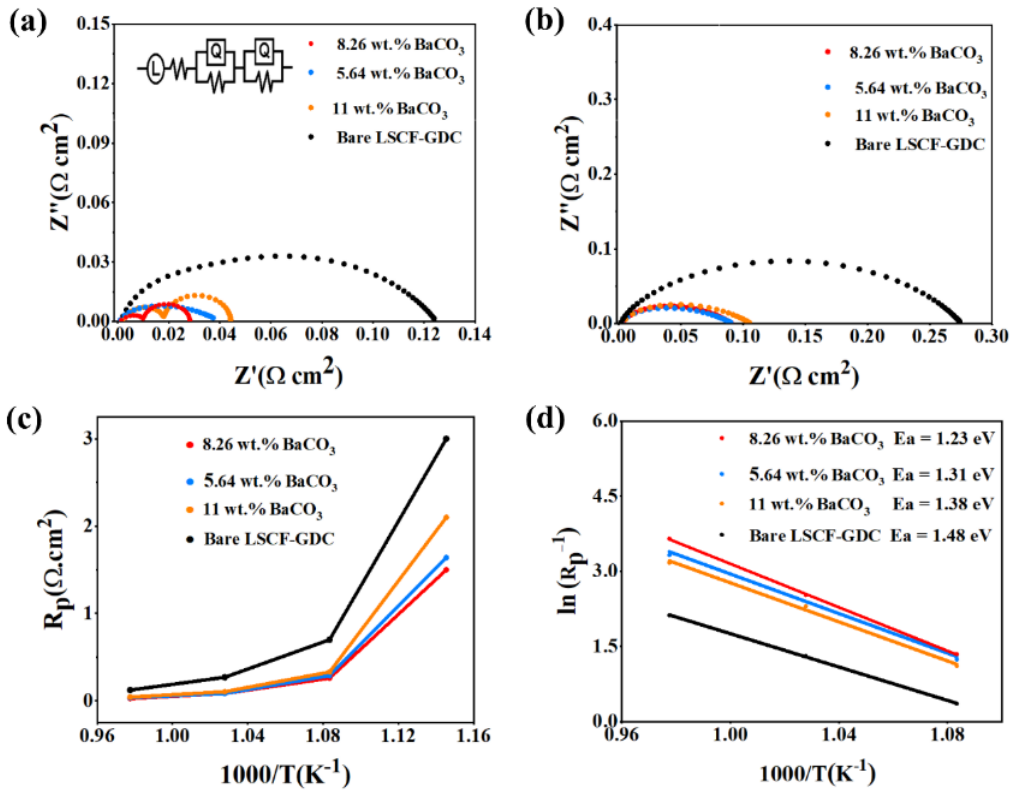

Figure 6. EIS spectra of the LSCF−GDC cathode with different loadings of $BaCO_3$; (**a**) 750 °C, (**b**) 700 °C, (**c**) R_p of the cathodes from 600−750 °C, and (**d**) corresponding Arrhenius plots.

Table 1 shows a comparison of the performances of anode-support single cells of SOFCs with different cathode materials reported in the literature. The performances listed are compared using the improving factor to minimize the effect of different electrolytes and fabrication processes. The improving factor of LSCF–GDC modified with $BaCO_3$ (56.6%) is lower compared to the reported values of LSCF–GDC modified with the active catalyst of $La_{0.6}Sr_{0.4}CoO_{3-\delta}$ (85.7%). However, generally speaking, the improvement factor of the present work is higher than those of the majority of the materials mentioned in Table 1. This high improvement factor suggests that $BaCO_3$ effectively enhanced the ORR at reduced temperatures for SOFCs.

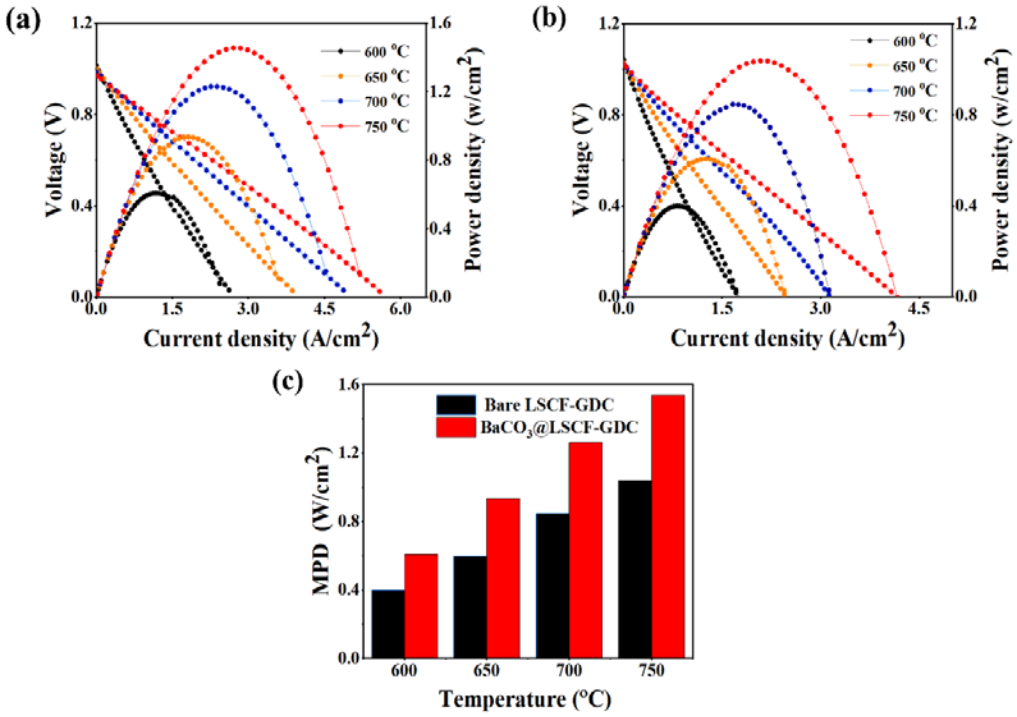

Figure 7. Power density curves of NiO-YSZ supported cell with (**a**) LSCF–GDC cathodes modified with 8.26 wt.% $BaCO_3$, (**b**) bare LSCF–GDC cathode, and (**c**) comparative maximum power density.

Table 1. Comparative performance of anode-support single cells of SOFCs with different cathodes reported in the literature.

Half Cell	Cathode + Infiltrated Material	MPD (W/cm^2) at 650 °C	Improving Factor (%)	Ref.
NiO-YSZ | YSZ | GDC	LSCF–GDC + $BaCO_3$	Bare: 0.6 Infiltrated: 0.94	56.6	This work
NiO-SDC | SDC	LSCF + CuO	Bare: 0.54 Infiltrated: 0.72	25	[31]
NiO-SDC | SDC	LSCF-SDC + CaO	Bare: 0.62 Infiltrated: 0.83	34.24	[35]
NiO-SDC | SDC	LSCF + CaO	Bare: 0.6 Infiltrated: 0.80	33.3	[35]
NiO-YSZ | YSZ | GDC	LSCF + CeO_2 (nanofiber)	Bare: 0.75 Infiltrated: 0.981	30	[43]
NiO-YSZ | YSZ | GDC	$(La_{0.6}Sr_{0.4})_{0.95}Co_{0.2}Fe_{0.8}O_{3-\delta}$ +$Pr_{0.8}Ce_{0.2}O_{2-\delta}$	Bare: 0.75 Infiltrated: 1.07	42.47	[44]
NiO-YSZ | YSZ | GDC	$(La_{0.6}Sr_{0.4})_{0.95}Co_{0.2}Fe_{0.8}O_{3-\delta}$ + $PrO_{2-\delta}$	Bare: 0.751 Infiltrated: 1.108	47.53	[44]
Ni-GDC | GDC	(LSCF–GDC) + $La_{0.6}Sr_{0.4}CoO_{3-\delta}$	Bare: 0.7 Infiltrated: 1.3	85.7	[45]

Figure 8 shows the EIS plots of the single cells operated with wet H_2 (~3% H_2O) as fuel and flowing air as the oxidant. The polarization resistance (R_p) of a single cell mainly comes from the cathode and anode, but the R_p value of the anode is negligible when wet H_2 (~3% H_2O) is used as fuel [46,47]. Therefore, the R_p values of the single cell predominantly correspond to the cathode side. Figure 8b shows the R_p values of the bare cathode are 1.00, 0.44, 0.19, and 0.1 Ω. cm^2 at 600, 650, 700, and 750 °C, respectively. In contrast, the R_p values of the 8.26 wt.% $BaCO_3$ nanoparticles-modified cathode are 0.38, 0.137, 0.093, and 0.054 Ω. cm^2 at 600, 650, 700, and 750 °C, respectively, as shown in Figure 8a. The corresponding values of ohmic resistance (R_o), polarization resistance

(R_p), and total resistance (R_t) of the single cell_modified and bare cathodes as a function of temperature are shown in Figure 8c,d, respectively. The ohmic resistance is the same for both cells, indicating that the main difference in the R_t value is predominantly associated with the cathode performance. This significant decrease in R_p can principally be attributed to the infiltration of $BaCO_3$ nanoparticles. The EIS result achieved with the single cell is slightly different from the symmetrical cell values. The slight difference may be associated with different working conditions of the single cell and symmetrical cells, and similar phenomena have also been observed by other researchers [48,49].

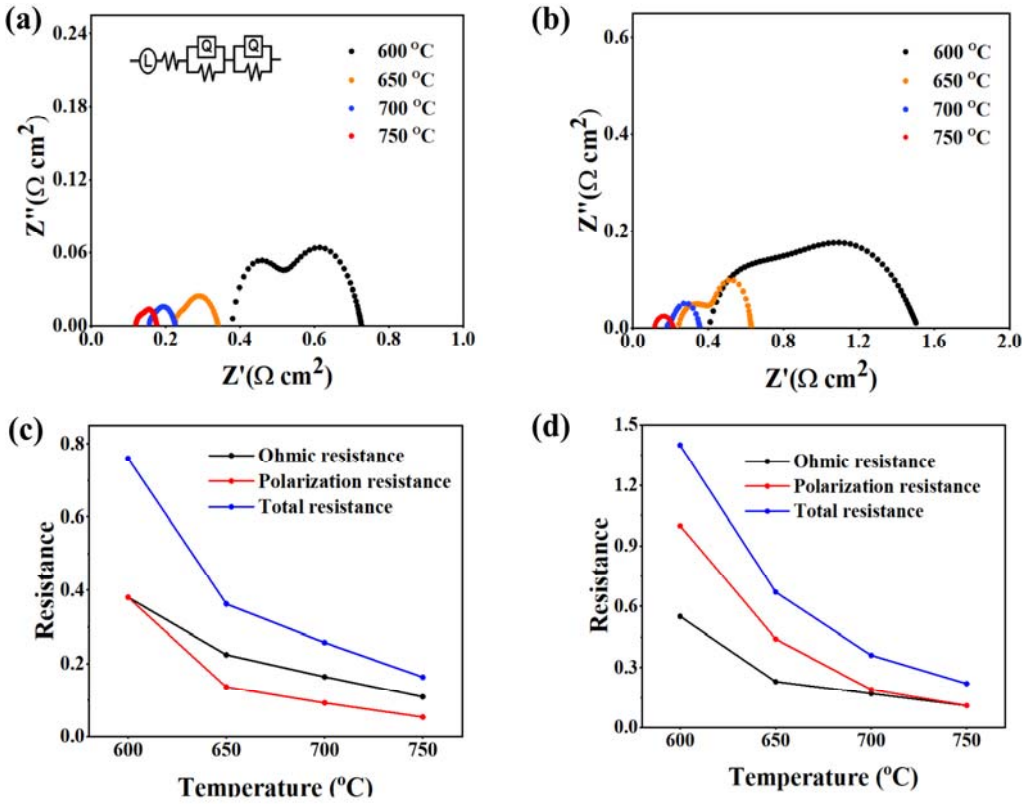

Figure 8. EIS plots of the single cell (**a**) $BaCO_3$ nanoparticles modified LSCF–GDC, (**b**) bare cathode, and corresponding values of R_o, R_p, and R_T of the impedance spectra of single cells with (**c**) modified cathodes, and (**d**) bare cathode.

Recently, several efforts have been devoted to the understanding of surface engineering of electrode materials to enhance their performance [50,51]. The first-principles method based on density functional theory (DFT) is used to verify surface engineering via understanding the mechanism by which $BaCO_3$ promotes ORR performance on SOFC electrode materials. Because the chemical formulas of $La_{0.6}Sr_{0.4}Co_{0.2}Fe_{0.8}O_{3-\delta}$ (LSCF) and $Gd_{0.2}Ce_{0.8}O_{2-\delta}$ (GDC) are complex, to simplify the calculation, $LaFeO_3$ and CeO_2 have been selected to represent LSCF and GDC, respectively. According to the XRD patterns shown in Figure 2, the $LaFeO_3$ crystal face (110), the CeO_2 crystal face (111), and the $BaCO_3$ crystal face (111) were constructed as a substrate for oxygen molecule adsorption. The bond length of the free oxygen molecule ($R_{O\text{-}O}$) is about 1.21 Å. In Figure 9a,b, when an oxygen molecule is placed on the surface of $LaFeO_3$ and CeO_2 for structural optimization, the $R_{O\text{-}O}$ values are 1.36 Å and 1.56 Å, respectively. Although here, the $R_{O\text{-}O}$ has increased, it still maintains the integrity of the oxygen molecule. Additionally, the distances between the O_2 molecule and the $LaFeO_3$/CeO_2 substrates (*d*) are 3.04 Å and 2.48 Å, respectively. Interestingly, when oxygen is adsorbed on the $BaCO_3$ crystal face (111), the $R_{O\text{-}O}$ increases to 4.05 Å, which is much larger than the 1.56 Å of $LaFeO_3$ and 1.36 Å of CeO_2, indicating that oxygen molecules dissociate spontaneously on the $BaCO_3$ surface, as shown in

Figure 9c. During this process, an oxygen molecule dissociates into two oxygen ions on the $BaCO_3$ crystal face (111). Moreover, Bader Charge analysis showed that oxygen molecules adsorbed on the $BaCO_3$ surface, 0.87 electrons transfer from the substrate to the oxygen ions during the adsorption process, which is larger than the 0.55 *e* and 0.54 *e* transferred from $LaFeO_3$ and CeO_2, respectively, suggests that a greater charge transfer contributes to the dissociation of oxygen molecules. As shown in Figure 9d, the charge density differences show that there is a yellow area around the oxygen, providing evidence that oxygen gets electrons from the $BaCO_3$ substrate, which is consistent with the Bader Charge analysis data. Therefore, as shown in Table 2 the calculated result shows that the introduction of $BaCO_3$ greatly promotes the dissociation of oxygen molecules, which induces the oxygen molecule to spontaneously dissociate into oxygen ions on its surface, thereby improving the ORR rate of the LSCF–GDC cathode material. This theoretical calculation explains why the introduction of $BaCO_3$ would improve the performance of SOFC cathode materials.

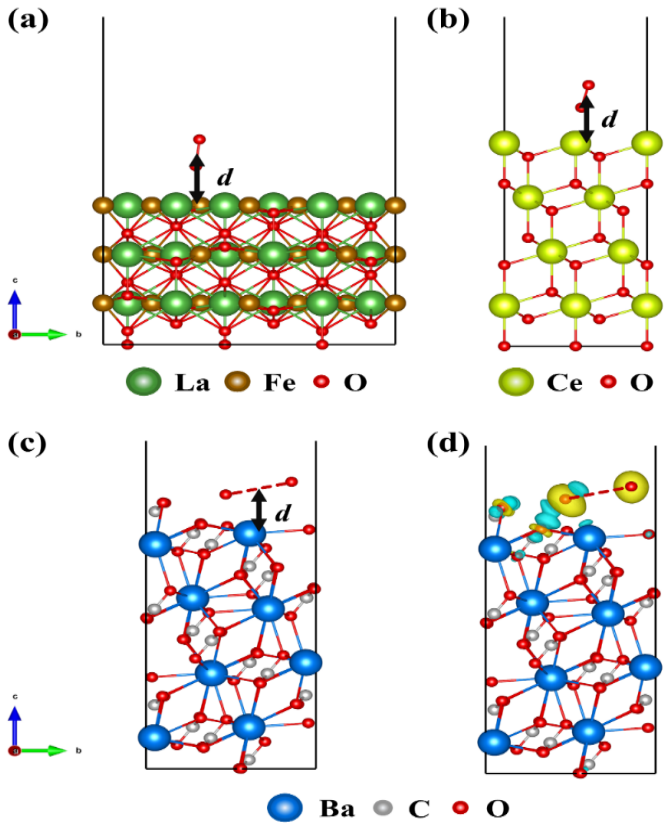

Figure 9. The structure of oxygen molecules when stably adsorbed on (**a**) the $LaFeO_3$ crystal face (110) and (**b**) the CeO_2 crystal face (111). (**c**) The structure of the oxygen molecules dissociated on the $BaCO_3$ crystal face (111). (**d**) Differential charge densities of oxygen molecule dissociation on the $BaCO_3$ crystal face (111).

Table 2. The distance of the O_2 molecule and substrates (*d*), the bond length of the O_2 molecule ($R_{O\text{-}O}$), and the charge of each O atom and O_2 molecule.

	d (Å)	$R_{O\text{-}O}$ (Å)	O_1 (*e*)	O_2 (*e*)	Sum (*e*)
$LaFeO_3$	3.04	1.56	−0.08	−0.47	−0.55
CeO_2	2.48	1.36	−0.14	−0.40	−0.54
$BaCO_3$	2.61	4.05	−0.41	−0.46	−0.87

3. Experimental Section

3.1. Sample Preparation

The $La_{0.6}Sr_{0.4}Co_{0.2}Fe_{0.8}O_{3-\delta}$ (LSCF) and $Gd_{0.2}Ce_{0.8}O_{2-\delta}$ (GDC) powders were synthesized using a modified Pechini method [52,53]. A Stoichiometric of La $(NO_3)_3{\cdot}6H_2O$, Sr $(NO_3)_3$, Co $(NO_3)_3{\cdot}6H_2O$, and Fe $(NO_3)_3{\cdot}9H_2O$ were dissolved in distilled water. Subsequently, citric acid as a chelating agent was added at a 1.5:1 ratio of citric acid to total metal ions. Ammonia solution was added to adjust the pH value of the solutions to ~7.0. The precursor solution was heated in a hotplate oven until the self-combustion was completed. The GDC powder was also synthesized using a similar procedure to the LSCF powders. To synthesize the desired $Gd_{0.2}Ce_{0.8}O_{2-\delta}$ (GDC), first, Gd_2O_3 was dissolved in the appropriate nitric acid (HNO_3) and $Ce(NO_3)_3{\cdot}6H_2O$ was dissolved in distilled water, followed by mixing both of the solutions. Finally, the resulting precursors were calcined at 700 and 1000 °C for 3 h to get the desired GDC and LSCF powders, respectively. The LSCF powder was homogeneously mixed with GDC powders (60:40 wt.%) in weight ratio, using a ball milling technique to prepare LSCF–GDC composite powders.

3.2. Cell Fabrication and Electrochemical Testing

For electrochemical impedance spectrum (EIS) studies, symmetrical cells with the configuration of LSCF–GDC | GDC buffer layer | YSZ | GDC buffer layer | LSCF–GDC were fabricated. The dense YSZ electrolyte was prepared via uniaxial pressing of the 8%, YSZ powder under 250 MPa and sintered at 1450 °C, for 10 h. The GDC and LSCF–GDC powders were homogeneously mixed with 5 wt.% and 10 wt.% ethyl cellulose in terpineol to prepare buffer layer and cathode slurries, respectively. The resulting buffer layer (GDC) slurries were coated onto the YSZ pellets and then, as-fabricated symmetric cells were sintered at 1300 °C, for 3 h. Finally, as-prepared cathode slurries were coated on the sintered GDC and co-sintered at 1000 °C, for 3 h.

The fuel cell performance was measured using an anode-supported cell of NiO-YSZ | YSZ | GDC | LSCF–GDC configuration. Anode mixtures containing NiO, YSZ, and starch (as pore former) were first mixed with a 6:4:2 weight ratio, respectively. The prepared anode precursors were pressed at 220 MPa and pre-fired at 1000 °C, for 3 h to obtain green pellets. The electrolyte (YSZ) slurry was also prepared using a similar process as the GDC buffer layer slurries as described earlier for the fabrication of symmetrical cells. The electrolyte slurries were spin-coated on the sintered anode pellet and co-sintered at 1400 °C, for 10 h. The GDC buffer layer slurries were coated onto the dense YSZ electrolyte and followed by sintering at 1300 °C. Finally, cathode slurries were coated on the GDC buffer layer and co-sintered at 1000 °C, to prepare a single with an area of cathode 0.2 cm^2.

The surface of the prepared single and symmetrical cells was modified via $BaCO_3$ nanoparticles using the solution infiltration process. An appropriate amount of Ba-$(OAc)_2$ was dissolved in the mixed solvent distilled water and ethanol at the volume ratio of 1:1, to prepare a 0.3 M Ba-$(OAc)_2$ precursor solution. As-prepared Ba-$(OAc)_2$ solution was infiltrated into the porous LSCF–GDC electrode, then calcined at 750 °C for 2 h. The $BaCO_3$ loading was calculated by determining the weight difference of the cathode before and after each infiltration cycle. The electrochemical measurements were examined using equipment from an IM6 electrochemical workstation (ZAHNER, Ursensollen, Germany). The EIS measurement was conducted over the frequency range of 0.01 Hz to 1 MHz with a signal amplitude of 5 mV. The performances of fuel cells were studied using an anode-supported single cell from 600 to 750 °C, where wet H_2 (~3% H_2O) as fuel was supplied to the anode side and the cathode side was exposed to the flowing air.

3.3. Characterization

Crystal structures of as-synthesized and chemical compatibility were examined by X-ray diffraction (XRD) with Cu-Ka radiation. The energy-dispersive X-ray spectroscopy (EDS) and field emission scanning electron microscope (FESEM, ZEISS Gemini300, Jena, Germany) were performed to examine the sample's elemental composition and microstruc-

ture, respectively. Thermogravimetric analysis (TGA) was carried out from 25 to 750 °C in the air to determine the thermal decomposition temperature of Ba-$(OAc)_2$. The electrochemical conductivity relaxation (ECR) was measured using a four-probe DC method, to analyze the chemical surface exchange (K_{chem}) of the sample. An appropriate weight of LSCF–GDC powders pressed was at 220 MPa, followed by sintering at 1200 °C for 5 h, to prepare a rectangular bar (~97%) (1.1 mm × 5 mm × 10 mm) with a density of about 97%. Furthermore, Ba-$(OAc)_2$ was infiltrated onto surfaces of the sintered LSCF–GDC bar and then heated at 750 °C for 2 h. The ECR was measured when the partial pressure of oxygen (P (O_2) changed from 0.2 to 1 atm, with a flow rate of 100 mL.min^{-1}, until a new equilibrium was achieved.

3.4. Computational Methods

Vienna ab initio simulation package (VASP) [54–56] based on DFT [57,58] was used for the first-principles calculations. Generalized-gradient-approximation (GGA) [59] was selected as the exchange-correlation function, and projected-augmented-wave (PAW) [60] was used as the pseudopotential to describe the interactions between ion and valence electrons. The *k*-point grid division of the Brillouin area adopts the Monkhorst–Pack [61] method. The *k*-point mesh was selected as 3 × 3 × 1, and the cut-off energy was 400 eV. The convergence standard of the interaction force between atoms is 0.01 eV. Å^{-1} and the convergence standard of energy is 10^{-5} eV. A vacuum layer of 15 Å was set along the perpendicular direction above the atomic slab to have avoided the influence of periodic conditions. The VESTA [62] software was used to display the structure.

4. Conclusions

In summary, this work demonstrates that $BaCO_3$ nanoparticles are successfully integrated into state-of-the-art LSCF–GDC cathode through the use of a solution-based infiltration of Ba-$(OAc)_2$, which promotes the remarkably enhanced electrochemical performance of SOFCs. The modified cathode has a polarization resistance (R_p) as low as 0.027 Ω cm^2 at 750 °C in a symmetrical cell and has a maximum power density of 1.48 W/cm^2 in a NiO-YSZ anode-support cell. This improvement can be attributed to the enhanced dissociation of an oxygen molecule by infiltration of the $BaCO_3$ nanoparticles, which accelerate the ORR kinetics values (K_{chem}). These explanations were confirmed by the DFT study, which shows that oxygen molecules dissociate spontaneously to form oxygen ions on the $BaCO_3$ surface, thereby improving the ORR rate of the cathode material. These results demonstrate that $BaCO_3$ nanoparticles have great potential to serve as an efficient solution for the surface modification of cathode materials for IT-SOFCs.

Author Contributions: Conceptualization, B.L. (Bin Lin), and H.G.D.; methodology, H.G.D., and Q.Y.; software, B.L. (Baihai Li) and Y.Y.; validation, B.L. (Baihai Li); formal analysis, H.G.D., S.Z. and K.S.; resources, D.T., X.L., Y.C. and B.L. (Bin Lin); data curation, H.G.D., and B.L. (Bin Lin); writing—original draft preparation, H.G.D.; writing—review and editing, B.L. (Bin Lin); visualization, H.G.D., and B.L. (Bin Lin); supervision, B.L. (Bin Lin) and D.T.; funding acquisition, B.L. (Bin Lin). All authors have read and agreed to the published version of the manuscript.

Funding: This research was funded by the Ministry of Science and Technology of China (2021YFE0100200), Pakistan Science Foundation (PSF) Project (PSF/CRP/18thProtocol (01)), the Fundamental Research Funds for the Central Universities of the University of Electronic Science and Technology of China (A03018023601020), the Foundation of Yangtze Delta Region Institute (Huzhou) of UESTC, China (U04210055), Research and Development Project of Anhui Province (201904a07020002), the Anhui Provincial Department of Education (gxbjZD2021074) and the Huainan Science and Technology Bureau (2018A374).

Data Availability Statement: Not applicable.

Conflicts of Interest: The authors declare no conflict of interest.

References

1. Wachsman, E.D.; Marlowe, C.A.; Lee, K.T. Role of solid oxide fuel cells in a balanced energy strategy. *Energy Environ. Sci.* **2012**, *5*, 5498–5509. [CrossRef]
2. Stambouli, A.B.; Traversa, E. Solid oxide fuel cells (SOFCs): A review of an environmentally clean and efficient source of energy. *Renew. Sustain. Energy Rev.* **2002**, *6*, 433–455. [CrossRef]
3. Niu, Y.; Zhou, Y.; Zhang, W.; Zhang, Y.; Evans, C.; Luo, Z.; Kane, N.; Ding, Y.; Chen, Y.; Guo, X.; et al. Highly active and durable air electrodes for reversible protonic ceramic electrochemical cells enabled by an efficient bifunctional catalyst. *Adv. Energy Mater.* **2022**, *12*, 2103783. [CrossRef]
4. Pirou, S.; Talic, B.; Brodersen, K.; Hauch, A.; Frandsen, H.L.; Skafte, T.L.; Persson, A.H.; Hogh, J.V.T.; Henriksen, H.; Navasa, M.; et al. Production of a monolithic fuel cell stack with high power density. *Nat. Commun.* **2022**, *13*, 1263. [CrossRef] [PubMed]
5. Xia, C.; Liu, M. Novel cathodes for low-temperature solid oxide fuel cells. *Adv. Mater.* **2002**, *14*, 521–523. [CrossRef]
6. Gao, Z.; Mogni, L.V.; Miller, E.C.; Railsback, J.G.; Barnett, S.A. A perspective on low-temperature solid oxide fuel cells. *Energy Environ. Sci.* **2016**, *9*, 1602–1644. [CrossRef]
7. Fang, J.; Meng, Z.; Li, J.; Du, Y.; Qin, Y.; Jiang, Y.; Bai, W.; Chase, G.G. The effect of operating parameters on regeneration characteristics and particulate emission characteristics of diesel particulate filters. *Appl. Therm. Eng.* **2019**, *148*, 860–867. [CrossRef]
8. Wang, S.F.; Lu, H.C.; Hsu, Y.F.; Jasinski, P. High-performance anode-supported solid oxide fuel cells with co-fired $Sm_{0.2}Ce_{0.8}O_{2-\delta}$ | $La_{0.8}Sr_{0.2}Ga_{0.8}Mg_{0.2}O_{-\delta}$ | $Sm_{0.2}Ce_{0.8}O_{2-\delta}$ sandwiched electrolyte. *Int. J. Hydrogen Energy* **2022**, *47*, 5429–5438. [CrossRef]
9. Wachsman, E.D.; Lee, K.T. Lowering the temperature of solid oxide fuel cells. *Science* **2011**, *334*, 935–939. [CrossRef]
10. Kan, W.H.; Samson, A.J.; Thangadurai, V. Trends in electrode development for next-generation solid oxide fuel cells. *J. Mater. Chem. A* **2016**, *4*, 17913–17932. [CrossRef]
11. Ascolani-Yael, J.; Montenegro-Hernandez, A.; Baque, L.C.; Toscani, L.M.; Caneiro, A.; Mogni, L.V. Oxygen diffusion and surface exchange coefficients of porous $La_{0.6}Sr_{0.4}Co_{0.2}Fe_{0.8}O_{3-\delta}$ decorated with Co_3O_4 nanoparticles. *J. Electrochem. Soc.* **2022**, *169*, 034514. [CrossRef]
12. Shi, Y.; Wen, Y.; Huang, K.; Xiong, X.; Wang, J.; Liu, M.; Ding, D.; Chen, Y.; Liu, T. Surface enhanced performance of $La_{0.6}Sr_{0.4}Co_{0.2}Fe_{0.8}O_{3-\delta}$ cathodes by infiltration Pr-Ni-Mn-O progress. *J. Alloys Compd.* **2022**, *902*, 163337. [CrossRef]
13. Sun, C.; Hui, R.; Roller, J. Cathode materials for solid oxide fuel cells: A review. *J. Solid State Electrochem.* **2010**, *14*, 1125–1144. [CrossRef]
14. Shao, Z.; Zhou, W.; Zhu, Z. Advanced synthesis of materials for intermediate-temperature solid oxide fuel cells. *Prog. Mater. Sci.* **2012**, *57*, 804–874. [CrossRef]
15. Jaiswal, N.; Tanwar, K.; Suman, R.; Kumar, D.; Upadhyay, S.; Parkash, O. A brief review on ceria-based solid electrolytes for solid oxide fuel cells. *J. Alloys Compd.* **2019**, *781*, 984–1005. [CrossRef]
16. Ni, N.; Xiao, W.; Zheng, C.; Jiang, J.; Yu, Y.; Hao, W.; Tang, M.; Shen, H.; Peng, D. Flash cosintering of a lanthanum strontium cobalt ferrite nanofibre/Gd-doped ceria bilayer structure. *J. Eur. Ceram. Soc.* **2022**, *42*, 2870–2878. [CrossRef]
17. Zhang, S.L.; Shang, Y.B.; Li, C.X.; Li, C.J. Vacuum cold sprayed nanostructured $La_{0.6}Sr_{0.4}Co_{0.2}Fe_{0.8}O_{3-\delta}$ as a high-performance cathode for porous metal-supported solid oxide fuel cells operating below 600 degrees C. *Mater. Today Energy* **2021**, *21*, 100815. [CrossRef]
18. Liu, M.; Ding, D.; Blinn, K.; Li, X.; Nie, L.; Liu, M. Enhanced performance of LSCF cathode through surface modification. *Int. J. Hydrogen Energy* **2012**, *37*, 8613–8620. [CrossRef]
19. Ding, D.; Li, X.; Lai, S.Y.; Gerdes, K.; Liu, M. Enhancing SOFC cathode performance by surface modification through infiltration. *Energy Environ. Sci.* **2014**, *7*, 552–575. [CrossRef]
20. Jiang, Z.; Xia, C.; Chen, F. Nano-structured composite cathodes for intermediate-temperature solid oxide fuel cells via an infiltration/impregnation technique. *Electrochim. Acta* **2010**, *55*, 3595–3605. [CrossRef]
21. Jiang, S.P. Nanoscale and nano-structured electrodes of solid oxide fuel cells by infiltration: Advances and challenges. *Int. J. Hydrogen Energy* **2012**, *37*, 449–470. [CrossRef]
22. dos Santos-Gómez, L.; Porras-Vázquez, J.; Losilla, E.; Martín, F.; Ramos-Barrado, J.; Marrero-López, D. Stability and performance of $La_{0.6}Sr_{0.4}Co_{0.2}Fe_{0.8}O_{3-\delta}$ nanostructured cathodes with $Ce_{0.8}Gd_{0.2}O_{1.9}$ surface coating. *J. Power Source* **2017**, *347*, 178–185. [CrossRef]
23. Song, Y.-H.; Rehman, S.U.; Kim, H.-S.; Song, H.-S.; Song, R.-H.; Lim, T.-H.; Hong, J.-E.; Park, S.-J.; Huh, J.-Y.; Lee, S.-B. Facile surface modification of LSCF | GDC cathodes by epitaxial deposition of $Sm_{0.5}Sr_{0.5}CoO_3$ via ultrasonic spray infiltration. *J. Mater. Chem. A* **2020**, *8*, 3967–3977. [CrossRef]
24. DiGiuseppe, G.; Boddapati, V. Characterization of solid oxide fuel cells with LSCF-SDC composite cathodes. *J. Energy* **2018**, *2018*, 1–7. [CrossRef]
25. Samreen, A.; Galvez-Sanchez, M.; Steinberger-Wilckens, R.; Arifin, N.A.; Saher, S.; Ali, S.; Qamar, A. Electrochemical performance of novel NGCO-LSCF composite cathode for intermediate temperature solid oxide fuel cells. *Int. J. Hydrogen Energy* **2020**, *45*, 21714–21721. [CrossRef]

26. Liu, Y.; Bi, J.; Chi, B.; Pu, J.; Jian, L. Effects of impregnating palladium on catalytic performance of LSCF-GDC composite cathodes for intermediate temperature solid oxide fuel cells. *Int. J. Hydrogen Energy* **2016**, *41*, 6486–6492. [CrossRef]
27. Sakito, Y.; Hirano, A.; Imanishi, N.; Takeda, Y.; Yamamoto, O.; Liu, Y. Silver infiltrated $La_{0.6}Sr_{0.4}Co_{0.2}Fe_{0.8}O_3$ cathodes for intermediate temperature solid oxide fuel cells. *J. Power Source* **2008**, *182*, 476–481. [CrossRef]
28. Wang, H.; Zhang, X.; Zhang, W.; Wei, Z.; Guan, K.; Meng, J.; Meng, F.; Meng, J.; Liu, X. Enhancing catalysis activity of $La_{0.6}Sr_{0.4}Co_{0.8}Fe_{0.2}O_{3-\delta}$ cathode for solid oxide fuel cell by a facile and efficient impregnation process. *Int. J. Hydrogen Energy* **2019**, *44*, 13757–13767. [CrossRef]
29. Paige, J.M.; Cheng, Y.; Pepin, P.A.; Curran, C.D.; Sun, D.; Chen, M.U.; McIntosh, S.; Vohs, J.M.; Gorte, R.J. Surface modification of SOFC cathodes by Co, Ni, and Pd oxides. *Solid State Ion.* **2019**, *341*, 115051. [CrossRef]
30. Nadeem, M.; Hu, B.; Xia, C. Effect of NiO addition on oxygen reduction reaction at lanthanum strontium cobalt ferrite cathode for solid oxide fuel cell. *Int. J. Hydrogen Energy* **2018**, *43*, 8079–8087. [CrossRef]
31. Hong, T.; Brinkman, K.; Xia, C. Copper oxide as a synergistic catalyst for the oxygen reduction reaction on $La_{0.6}Sr_{0.4}Co_{0.2}Fe_{0.8}O_{3-\delta}$ perovskite structured electrocatalyst. *J. Power Source* **2016**, *329*, 281–289. [CrossRef]
32. Yang, Y.; Li, M.; Ren, Y.; Li, Y.; Xia, C. Magnesium oxide as synergistic catalyst for oxygen reduction reaction on strontium doped lanthanum cobalt ferrite. *Int. J. Hydrogen Energy* **2018**, *43*, 3797–3802. [CrossRef]
33. Li, M.; Sun, Z.; Yang, W.; Hong, T.; Zhu, Z.; Zhang, Y.; Wu, X.; Xia, C. Mechanism for the enhanced oxygen reduction reaction of $La_{0.6}Sr_{0.4}Co_{0.2}Fe_{0.8}O_{3-\delta}$ by strontium carbonate. *Phys. Chem. Chem. Phys.* **2017**, *19*, 503–509. [CrossRef] [PubMed]
34. Hong, T.; Lee, S.; Ohodnicki, P.; Brinkman, K. A highly scalable spray coating technique for electrode infiltration: Barium carbonate infiltrated $La_{0.6}Sr_{0.4}Co_{0.2}Fe_{0.8}O_{3-\delta}$ perovskite structured electrocatalyst with demonstrated long term durability. *Int. J. Hydrogen Energy* **2017**, *42*, 24978–24988. [CrossRef]
35. Zhang, L.; Hong, T.; Li, Y.; Xia, C. CaO effect on the electrochemical performance of lanthanum strontium cobalt ferrite cathode for intermediate-temperature solid oxide fuel cell. *Int. J. Hydrogen Energy* **2017**, *42*, 17242–17250. [CrossRef]
36. Hong, T.; Brinkman, K.S.; Xia, C. Barium carbonate nanoparticles as synergistic catalysts for the oxygen reduction reaction on $La_{0.6}Sr_{0.4}Co_{0.2}Fe_{0.8}O_{3-\delta}$ solid-oxide fuel cell cathodes. *ChemElectroChem* **2016**, *3*, 805–813. [CrossRef]
37. Desta, H.G.; Yang, Y.; Teketel, B.S.; Yang, Q.; Song, K.; Zhu, S.; Tian, D.; Chen, Y.; Luo, T.; Lin, B. Enhanced performance of $La_{0.8}Sr_{0.2}FeO_{3-\delta}$-$Gd_{0.2}Ce_{0.8}O_{2-\delta}$ cathode for solid oxide fuel cells by surface modification with $BaCO_3$ nanoparticles. *Micromachines* **2022**, *13*, 884. [CrossRef]
38. Hwang, U.-Y.; Park, H.-S.; Koo, K.-K. Behavior of barium acetate and titanium isopropoxide during the formation of crystalline barium titanate. *Ind. Eng. Chem. Res.* **2004**, *43*, 728–734. [CrossRef]
39. Joh, D.W.; Rath, M.K.; Park, J.W.; Park, J.H.; Cho, K.H.; Lee, S.; Yoon, K.J.; Lee, J.-H.; Lee, K.T. Sintering behavior and electrochemical performances of nano-sized gadolinium-doped ceria via ammonium carbonate assisted co-precipitation for solid oxide fuel cells. *J. Alloys Compd.* **2016**, *682*, 188–195. [CrossRef]
40. Nie, L.; Liu, M.; Zhang, Y.; Liu, M. $La_{0.6}Sr_{0.4}Co_{0.2}Fe_{0.8}O_{3-\delta}$ cathodes infiltrated with samarium-doped cerium oxide for solid oxide fuel cells. *J. Power Source* **2010**, *195*, 4704–4708. [CrossRef]
41. Joh, D.W.; Cha, A.; Park, J.H.; Kim, K.J.; Bae, K.T.; Kim, D.; Choi, Y.K.; An, H.; Shin, J.S.; Yoon, K.J. In situ synthesized $La_{0.6}Sr_{0.4}Co_{0.2}Fe_{0.8}O_{3-\delta}$-$Gd_{0.1}Ce_{0.9}O_{1.95}$ nanocomposite cathodes via a modified sol-gel process for intermediate temperature solid oxide fuel cells. *ACS Appl. Nano Mater.* **2018**, *1*, 2934–2942. [CrossRef]
42. Gao, Z.; Barnett, S.A. Reduced-temperature firing of anode-supported solid oxide fuel cells. *ECS Trans.* **2013**, *58*, 231. [CrossRef]
43. Zhang, W.; Wang, H.; Guan, K.; Wei, Z.; Zhang, X.; Meng, J.; Liu, X.; Meng, J. $La_{0.6}Sr_{0.4}Co_{0.2}Fe_{0.8}O_{3-\delta}/CeO_2$ Heterostructured composite nanofibers as a highly active and robust cathode catalyst for solid oxide fuel cells. *ACS Appl. Mater. Interfaces* **2019**, *11*, 26830–26841. [CrossRef] [PubMed]
44. Wang, H.; Zhang, W.; Guan, K.; Wei, Z.; Meng, J.; Meng, J.; Liu, X. Enhancing activity and durability of A-Site-deficient $(La_{0.6}Sr_{0.4})_{0.95}Co_{0.2}Fe_{0.8}O_{3-\delta}$ cathode by surface modification with $PrO_{2-\delta}$ nanoparticles. *ACS Sustain. Chem. Eng.* **2020**, *8*, 3367–3380. [CrossRef]
45. Huang, Y.L.; Hussain, A.M.; Wachsman, E.D. Nanoscale cathode modification for high performance and stable low-temperature solid oxide fuel cells (SOFCs). *Nano Energy* **2018**, *49*, 186–192. [CrossRef]
46. Xia, C.; Liu, M. Microstructures, conductivities, and electrochemical properties of $Ce_{0.9}Gd_{0.1}O_2$ and GDC-Ni anodes for low-temperature SOFCs. *Solid State Ion.* **2002**, *152*, 423–430. [CrossRef]
47. Van Herle, J.; Ihringer, R.; Cavieres, R.V.; Constantin, L.; Bucheli, O. Anode supported solid oxide fuel cells with screen-printed cathodes. *J. Eur. Ceram. Soc.* **2001**, *21*, 1855–1859. [CrossRef]
48. Ling, Y.; Lu, X.; Niu, J.; Chen, H.; Ding, Y.; Ou, X.; Zhao, L. Antimony doped barium strontium ferrite perovskites as novel cathodes for intermediate-temperature solid oxide fuel cells. *J. Alloys Compd.* **2016**, *666*, 23–29. [CrossRef]
49. Yang, Y.; Li, R.; Wu, Y.; Chu, Y.; Tian, D.; Lu, X.; Guo, L.; Lin, B.; Feng, P.; Ling, Y. Highly active self-assembled hybrid catalyst with multiphase heterointerfaces to accelerate cathodic oxygen reduction of intermediate-temperature solid oxide fuel cells. *Ceram. Int.* **2020**, *46*, 9661–9668. [CrossRef]
50. Ali, T.; Qiao, W.; Zhang, D.; Liu, W.; Sajjad, S.; Yan, C.; Su, R. Surface Sulfur Vacancy Engineering of Metal Sulfides Promoted Desorption of Hydrogen Atoms for Enhanced Electrocatalytic Hydrogen Evolution. *J. Phys. Chem. C* **2021**, *125*, 12707–12712. [CrossRef]

51. Ali, T.; Wang, X.; Tang, K.; Li, Q.; Sajjad, S.; Khan, S.; Farooqi, S.A.; Yan, C. SnS_2 Quantum Dots Growth on MoS_2: Atomic-Level Heterostructure for Electrocatalytic Hydrogen Evolution. *Electrochim. Acta* **2019**, *300*, 45–52. [CrossRef]
52. Pechini, M.P. Method of Preparing Lead and Alkaline Earth Titanates and Niobates and Coating Method Using the Same to Form a Capacitor. Google Patents No.US3330697A, 26 September 1967.
53. Tian, D.; Lin, B.; Yang, Y.; Chen, Y.; Lu, X.; Wang, Z.; Liu, W.; Traversa, E. Enhanced performance of symmetrical solid oxide fuel cells using a doped ceria buffer layer. *Electrochim. Acta* **2016**, *208*, 318–324. [CrossRef]
54. Kresse, G.; Hafner, J. Ab initio molecular-dynamics simulation of the liquid-metal-amorphous-semiconductor transition in germanium. *Phys. Rev. B* **1994**, *49*, 14251–14269. [CrossRef]
55. Kresse, G.; Furthmüller, J. Efficient iterative schemes for ab initio total-energy calculations using a plane-wave basis set. *Phys. Rev. B* **1996**, *54*, 11169. [CrossRef]
56. Kresse, G.; Furthmuller, J. Efficiency of ab-initio total energy calculations for metals and semiconductors using a plane-wave basis set. *Comput. Mater. Sci.* **1996**, *6*, 15–50. [CrossRef]
57. Liechtenstein, A.I.; Anisimov, V.I.; Zaanen, J. Density-functional theory, and strong interactions: Orbital ordering in Mott-Hubbard insulators. *Phys. Rev. B* **1995**, *52*, R5467–R5470. [CrossRef]
58. Neuhauser, D.; Baer, R.; Rabani, E. Communication: Embedded fragment stochastic density functional theory. *J. Chem. Phys.* **2014**, *141*, 041102. [CrossRef]
59. Perdew, J.P.; Burke, K.; Ernzerhof, M. Generalized Gradient Approximation Made Simple. *Phys. Rev. Lett.* **1998**, *77*, 3865–3868. [CrossRef]
60. Blöchl, P.E. Projector augmented-wave method. *Phys. Rev. B* **1994**, *50*, 17953. [CrossRef]
61. Monkhorst, H.J.; Pack, J.D. Special points for Brillouin-zone integrations. *Phys. Rev. B* **1976**, *13*, 5188. [CrossRef]
62. Momma, K.; Izumi, F. VESTA: A three-dimensional visualization system for electronic and structural analysis. *J. Appl. Crystallogr.* **2008**, *41*, 653–658. [CrossRef]